Journal of Power Sources 193 (2009) 706–712

Contents lists available at ScienceDirect

Journal of Power Sources

journal homepage: www.elsevier.com/locate/jpowsour

Fabrication and evaluation of solid-oxide fuel cell anodes employing reaction-sintered yttria-stabilized zirconia

Daniel Storjohann[a], James Daggett[b], Neal P. Sullivan[a,*], Huayang Zhu[a], Robert J. Kee[a], Sophie Menzer[c], Dustin Beeaff[c]

[a] Engineering Division, Colorado School of Mines, Golden, CO 80401, USA
[b] Protonex Technology Corporation, Broomfield, CO 80020, USA
[c] Fuel Cell Division, CoorsTek, Inc., Golden, CO 80401, USA

ARTICLE INFO

Article history:
Received 13 March 2009
Received in revised form 15 April 2009
Accepted 15 April 2009
Available online 24 April 2009

Keywords:
SOFC
Anode
YSZ

ABSTRACT

This paper reports on the fabrication and performance of solid-oxide fuel cell (SOFC) anodes utilizing yttria reaction-sintered zirconia (YRSZ). Through the reaction-sintering process, the technical-grade YSZ commonly used in the Ni–YSZ anode cermet is replaced with lower-cost ZrO_2 and Y_2O_3 materials. When sintered in the presence of nickel oxide, ZrO_2 and Y_2O_3 form cubic-phase YSZ at temperatures characteristic of SOFC processing (1400–1550 °C). Reaction sintering enables the formation of YSZ during cell fabrication, reducing SOFC anode raw-materials cost and the number of SOFC-fabrication processes. This paper reports the results of a broad range of characterization and performance measurements to evaluate the YRSZ material, including (1) crystal structure, (2) morphology, (3) pore-size distribution, (4) electronic resistivity, (5) fracture strength, (6) gas transport and catalytic activity, and (7) electrochemical performance. Material properties and performance are found to be comparable to or better than equivalent materials fabricated by conventional processes.

1. Introduction

The objective of this paper is to introduce and characterize a novel method to fabricate Ni–YSZ ceramic–metallic composite (cermet) anode structures for solid-oxide fuel cell (SOFC) applications. Yttria reaction-sintered zirconia (YRSZ) promises significant reduction in cost, yet delivers comparable functional performance compared to traditionally fabricated Ni–YSZ. After first discussing the fabrication method, the paper reports the results of a wide range of performance-characterization techniques.

The most-common anode material used in solid-oxide fuel cells (SOFCs) is a ceramic–metallic composite comprised of 50 vol% nickel and 50 vol% yttria-stabilized zirconia (YSZ). During anode fabrication, cubic-phase YSZ powders are mixed with nickel oxide powders (NiO) and sintered to form the anode support. To reduce the cost of ceramic processing, the electrolyte layer is commonly co-sintered with the anode, with some developers also co-sintering the cathode layer as well [1].

The reaction-sintering process does not use YSZ in the anode formulation. Rather, the anode is fabricated from low-cost zirconia (ZrO_2), yttria (Y_2O_3) and NiO powders; the use of more-costly YSZ is limited to the thin electrolyte layer. When sintered in the presence of nickel oxide, the ZrO_2 and Y_2O_3 form cubic-phase YSZ at calcination temperatures that are characteristic of MEA-fabrication processes (1400–1550 °C) [2–4]. Co-sintering of the anode with the electrolyte remains unchanged. By forming the YSZ-phase of the anode during cell fabrication, reaction sintering reduces anode-YSZ materials cost to as low as \$10 kg^{-1}, well below current costs for conventional fabrication. Because the anode structure in anode-supported cell architectures constitutes 90% of the total material, reaction sintering promises to significantly reduce the overall cost of SOFC fabrication. Clearly, the NiO material also plays a role in defining MEA costs; the nickel oxide used in this study was purchased for \$10 kg^{-1}.

Although reducing materials and fabrication cost is certainly important, it cannot come at the expense of cell performance. To compare performance, nominally similar anodes are fabricated using conventional methods (i.e., beginning with YSZ powders) and using the reaction-sintering approach. The analysis includes (1) microstructural morphology using high-resolution microscopy, (2) crystal structure using X-ray diffraction, (3) porosity and pore structure using porosimetry, (4) electrical resistance using 4-point probes, (5) fracture strength using 4-point bending, (6) gas transport and catalytic reforming activity using a "Separated Anode Experiment," and (7) overall polarization performance of complete cells.

* Corresponding author. Tel: +1 303 273 3656; fax: +1 303 273 3602.
E-mail address: nsulliva@mines.edu (N.P. Sullivan).

0378-7753/$ – see front matter © 2009 Elsevier B.V. All rights reserved.
doi:10.1016/j.jpowsour.2009.04.026

2. Fabrication processes

2.1. Anode slurry formulations

Our conventional anode fabrication (designated "C-based") begins by combining 280 g of nickel oxide powder (Inco/Standard NiO), 150 g of 8YSZ powder (Tosoh Corporation/TZ8Y), 178 g of deionized water, and 1.8 g of dispersant (Darvan/821A), and mixing overnight in a plastic ball mill. After initial mixing, 44 g of binder (Baker/PVA 10% aqueous solution) is added, and the solution is mixed for an additional 3–4 h. No pore former is added.

The NiO-YRSZ fabrication (designated "RS-based") begins by combining and ball-milling 92 mol% monoclinic zirconia powder with 8 mol% yttria powder (Advanced Material Resources, Toronto, Ontario). After drying and screening, the yttria–zirconia powder mixture is then blended with 65 wt% nickel oxide (OMG, Westlake, OH). The anode powder is further mixed with different binders that depend upon the desired final anode-forming process: dry-pressing, roll-compaction, extrusion or slip casting. As with the conventional anode formulation, no pore former is added. The essential difference between the C- and RS-powder formulations is the direct incorporation of 8YSZ powders in the C-based anode, and zirconia and yttria powders in the RS-based approach.

The RS-based NiO powders have a particle size of 10 μm and a surface area of 70 $m^2\ g^{-1}$, while the C-based formulations utilize a finer NiO material (7 μm and 90 $m^2\ g^{-1}$). As will be shown through high-resolution microscopy and gas-transport measurements, this change contributes to the more open pore structure and more facile gas transport across the RS-based anodes.

2.2. Planar anode supports

Planar anodes are fabricated using both dry pressing and roll compaction. The conventional slurries are dried, crushed with a mortar and pestle, and sieved through a −325 mesh screen. To prepare the RS-powder formulations for dry pressing and roll compaction, the slurries are spray-dried in an 20.3-cm (8-in.) rotary atomizer. Following drying, the C- and RS-based powders are weighed into 10-g portions and pressed into disc-shaped powder compacts using a uni-axial press (Carver AutoFour30) loaded to 53.4 kN with a 10-s hold time. After pressing, the discs measure 5.72 cm (2.25 in.) in diameter and approximately 3.2 mm thick (0.125 in.). The powder compacts are placed onto YSZ–Al_2O_3 porous setter plates (Selee Ceramics), and sintered in air at a temperature between 1400 and 1550 °C for 4 h. These planar anodes are used to evaluate and compare morphology, porosity, pore-size distribution, gas transport and catalytic activity of the C- and RS-based materials. Modulus of Rupture (MOR) bars of the RS-based material are also fabricated by similar dry pressing and sintering processes.

2.3. Tubular anode supports

Tubular anodes are fabricated from both the C- and RS-based formulations using slip casting. Each anode slurry is poured into a plaster-of-paris mould and allowed to stand for 5–10 min. The slurry is drained from the mould, leaving a layer of anode material deposited on the walls; this deposit is dried at room temperature for 16 h. The shrinkage that occurs during drying allows the green anode tube to slide freely from the mould. These green anode tubes are then placed on a flat surface for 24 h to complete the drying process. RS-based tubular anode supports are also fabricated using extrusion. In both cases the tubular anodes are hang-fired at 1400 °C and sintered at 1550 °C. The tubular anodes are characterized by measuring pore-size distribution and electronic resistivity.

2.4. Tubular membrane–electrode assemblies

To fabricate complete RS-based MEAs, the dense electrolyte layer is spray-coated onto the green slip-cast RS-based anode tubes. The electrolyte-spray formulation uses 8 mol% yttria-stabilized zirconia powders (Tosoh, TZ8Y). To match the sintering shrinkage between the Tosoh YSZ powders and the RS-based anode supports, the Tosoh YSZ powder is calcined prior to spray coating [5]. After calcining, the partially sintered YSZ agglomerates are ball milled in polypropylene carboys using 12-mm high-purity ZrO_2 media for 4–10 h, and then wet milled in ethanol until a sub-micron D50 is achieved. After drying, the milled YSZ powder is sifted through an 80-mesh screen.

To form the electrolyte slurry on the RS-based anodes, screened YSZ powders are mixed with the binders, dispersants, and solvents, and then applied to the unfired RS-based tubular anodes using a pneumatic spray. The anode and electrolyte are hang-fired and co-sintered at a temperature between 1400 and 1550 °C for 4 h, resulting in an electrolyte that is approximately 20 μm thick.

The electrolyte application process differs slightly for the C-based MEAs. After drying, C-based tubes are vertically supported and bisque-fired in a kiln at 1050 °C for 1 h to begin the sintering process between ceramic particles, vaporize the processing additives, and provide handling strength for the electrolyte coating process. The electrolyte is applied to the bisque-fired tubes through dip-coating in a YSZ slurry; C-based tubes are then sintered for an additional 4.5 h at 1450 °C.

After co-sintering the anode–electrolyte assemblies, a thin porous cathode functional layer (CFL) is applied onto the electrolyte using brush coating. The CFL paste is a mixture of half (by weight) strontium-doped lanthanum manganate ($(La_{0.8}Sr_{0.2})_xMnO_{3-x}$, LSM) and half 8 mol% yttria-stabilized zirconia (Electro-Science Corporation, 4422). To improve current collection, a pure LSM porous layer is applied on top of the LSM-YSZ layer. The cathode-coated tubular cells are sintered in air at 1200 °C for 2 h, resulting in cathodes that are approximately 40 μm thick.

3. Materials characterization

3.1. Crystal structure

It is essential to demonstrate that cubic yttria-stabilized zirconia is formed as a result of sintering yttria and zirconia powders in the presence of nickel oxide. Indeed, this result is central to viability of the reaction-sintering process. X-ray diffraction (Scintag Pad-X diffractometer) is used to evaluate crystal structure at room temperature for both conventional and RS-based materials. As a further point of comparison, Y_2O_3/ZrO_2 powder mixtures that are sintered in the absence of nickel oxide are analyzed. Both materials are calcined at the same temperature.

Fig. 1 compares XRD patterns obtained from an RS-based anode with that of Y_2O_3/ZrO_2 powders co-sintered at 1500 °C. Showing a narrow range of angles (2θ) between 27° and 33° highlights the features for monoclinic (1 1 1) and tetragonal (1 0 1) zirconia phases. The dashed lines show that without NiO, the co-sintered zirconia-yttria powders do not fully form cubic YSZ. However, the solid lines show that the YRSZ material does not retain any features of the monoclinic zirconia. Because the cubic (1 1 1) and tetragonal (1 0 1) YSZ peaks around 30° are only 0.075° apart, it cannot be determined with certainty that only the cubic phase of yttria-stabilized zirconia is being obtained in either material. Nevertheless, it is clear that the Ni–YRSZ material shows no monoclinic zirconia phase.

Fig. 2 compares XRD patterns obtained from RS- and C-based anode supports (prior to NiO reduction). The lower panel shows reference peaks for pure NiO and cubic YSZ. It is evident that both materials have very similar crystal structures. These results indi-

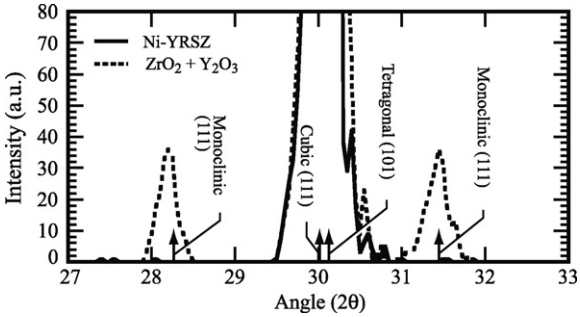

Fig. 1. XRD patterns obtained from a RS-based anode with that from a ZrO_2/Y_2O_3 powder mixture calcined at 1500 °C in the absence of nickel oxide. Locations of the reference peaks are shown for monoclinic and tetragonal zirconia and for cubic YSZ.

cate strongly that when calcined in the presence of nickel oxide, monoclinic yttria and zirconia powders form the desired cubic-phase yttria-stabilized zirconia at temperatures characteristic of SOFC processing.

3.2. Microstructural morphology

The microstructure of the anode–electrolyte interface is central to obtaining high SOFC electrochemical performance. To evaluate the microstructures resulting from alternative processing, anode structures and full membrane–electrode assemblies are characterized using high-resolution microscopy, liquid picnometry, and porosimetry.

The morphology of the C- and RS-based anodes and tubular RS-based MEAs are examined using scanning electron microscopy (SEM-JEOL JSM-6390). Prior to SEM analysis, anodes are exposed to a reducing environment (3.5% H_2, balance Ar) at 850 °C for 24 h. This process converts the nickel oxide within the anode to nickel, and increases the anode porosity. After reduction, anode porosities are determined using liquid picnometry and mercury porosimetry.

Fig. 3 shows fracture cross-sections of reduced C- and RS-based anodes that are fabricated by dry pressing. The conventional anode supports (Fig. 3a) reveal small particle sizes and fine porosity. This is in contrast with the significantly larger particle sizes and more-

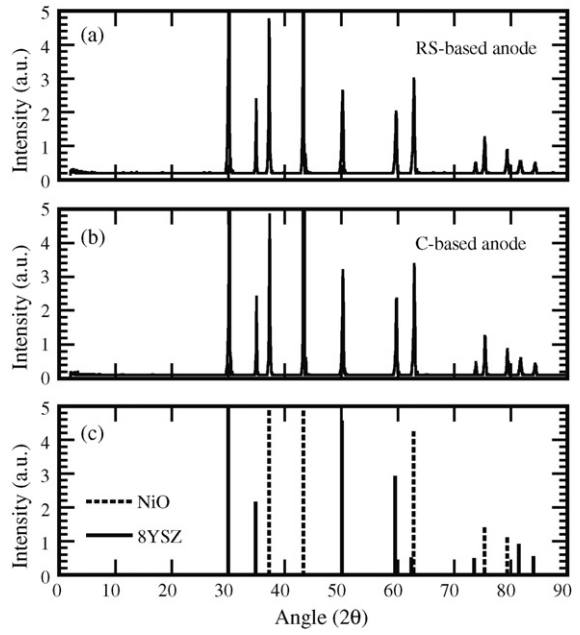

Fig. 2. Comparison of XRD patterns obtained from RS- and C-based anodes. The lower panel shows reference peaks for pure NiO and cubic-phase YSZ.

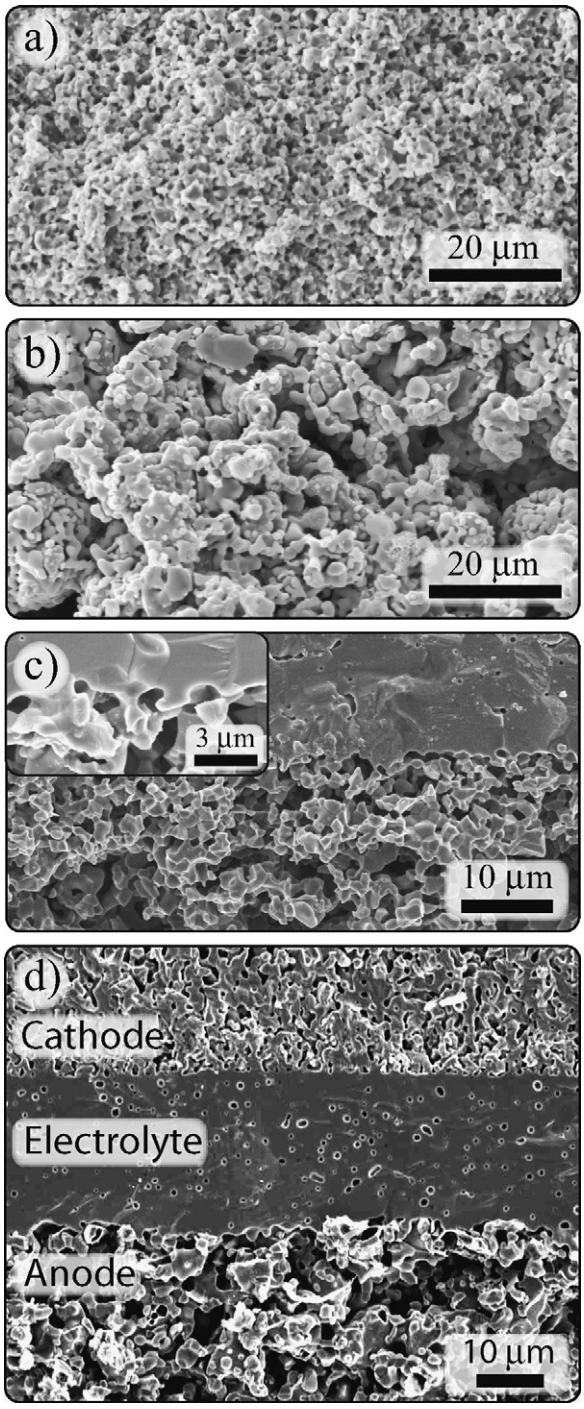

Fig. 3. SEM images of fracture cross-sections: (a) C-based anode; (b) RS-based anode; (c) RS-based anode–electrolyte assembly in which the nickel has been leeched from the anode; and (d) RS-based tubular membrane–electrode assembly. NiO in anodes has been reduced to nickel in images (a), (b), and (d).

open porosity that is evident in the RS-based anodes (Fig. 3b). Because no pore formers are added to either anode formulation, the open porosity is well distributed in both samples. The conventional material shows Ni and YSZ particles that are more uniform in size. Because of the comparatively larger initial particle size of the OMG NiO, the RS-based material has relatively coarse, connected, nickel grains that are surrounded by smaller YSZ particles.

Fig. 3c shows a micrograph of an RS-based anode–electrolyte assembly in which the nickel has been removed by leeching with nitric acid. This image shows that the YSZ grains

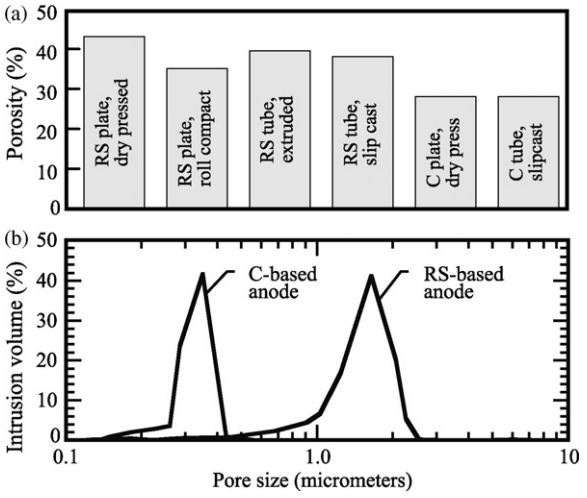

Fig. 4. (a) Open porosity of RS- and C-based anodes, as measured using Archimedes method; and (b) pore-size distribution in dry-pressed, reduced C- and RS-based anodes.

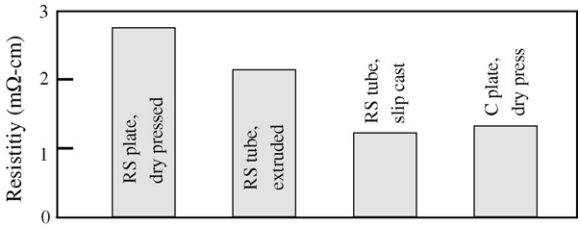

Fig. 5. Electronic resistivity of C- and RS-based anodes in a gas-phase reducing environment of 3.5% H_2 (balance Ar) at 800 °C.

are well-sintered, promoting facile ion conduction and enhancing mechanical strength. Additionally, the bonding and necking between the electrolyte and the anode is extensive, again facilitating ion conduction from the dense electrolyte into the cermet anode structure.

Fig. 3d is a micrograph of an RS-based tubular membrane–electrode assembly. The sprayed electrolyte is approximately 20 μm thick, and shows some measure of porosity. The cathode is also well-sintered to the electrolyte, with fine feature sizes and porosity. No undesirable phases appear to form from reactions between the RS-based anode material and the YSZ electrolyte material.

This series of images qualitatively indicate that the RS-based anode is chemically compatibility with the 8YSZ electrolyte material. Some pores are apparent in the dense electrolyte. However, based on measure open-circuit potential in full cells, it appears that pores are not connected and that the electrolyte is impermeable to any gas leakage.

Fig. 4a shows the open porosity of reduced RS-based anodes that are fabricated by dry pressing, roll compaction, extrusion, and slip casting. These measurements are made using liquid picnometry (Archimedes method) in water. The YRSZ materials have porosities ranging between 35 and 43%. Porosity of conventionally processed anodes is somewhat lower at approximately 28%.

Pore-size distribution is measured by mercury porosimetry (Micromeritics Autopore II, Model 9220) [6,7]. Fig. 4b shows that 95% of pores in the RS-based supports are around 1–2 μm in size, while pore-sizes for C-based material ranges between 0.2 and 0.4 μm. Similar pore-sizes and ranges are found in RS-based anodes fabricated by roll compaction and extrusion. These porosity and pore-size distribution measurements are consistent with the microscopy shown in Fig. 3, and promote gas transport across the RS-based anodes.

3.3. Electronic resistivity

Electronic resistivity of C- and RS-based anode tubes is determined using a four-point probe technique (Agilent 4338B Milliohmeter). Nickel wires (0.6-mm diameter) are first wrapped around each end of sintered, unreduced, C- and RS-based anode supports, and then bonded to the tubes using NiO paste (ElectroScience Corporation, 4410). For the RS-based anodes, measurements are made for dry-pressed plates, extruded tubes and slip-cast tubes. For the conventional anodes, measurements are made only for slip-cast tubes.

The assemblies are placed in a tube furnace (Thermolyne 21100) and exposed to a reducing environment (3.5% H_2 in Ar) at 850 °C, which reduces the nickel oxide in the anode support and the contact paste to nickel. All resistivity data are corrected for the residual resistivity of the leads by subtracting the short-circuit value from the specimen value.

Fig. 5 shows the electronic resistivities of C- and RS-based anodes. These results are measured at 800 °C in a reducing environment (3.5 mol% H_2, balance Ar). Resistivities ranging between 1.2 and 2.7 mΩ cm are comparable to published values [8]. The resistivity of reaction-sintered anodes is comparable to that of the conventional anode supports, and adequate for electron transport in SOFC applications.

3.4. Fracture strength

The fracture strength of the RS-based anodes is measured through controlled fracture of modulus-of-rupture (MOR) bars. Bars are initially fabricated using dry pressing; the bars are ground on four sides using a diamond wheel to achieve dimensions of 4 mm × 2.7 mm. Fracture strength is measured at room temperature using the four-point bend technique with a strain rate of 0.5 mm min^{-1} and a lower load span of 40 mm, in accordance with ASTM C1161 [9].

The average fracture strength of dry-pressed, reduced, Ni–YRSZ MOR bars is 100 MPa, with a Weibull modulus of 6. Porosity of the MOR bars reaches 40% for the reduced anode, corresponding to the highest porosity of the Ni–YRSZ material. Previously reported fracture strength for Ni–8YSZ anodes range from 56 to 140 MPa, and vary with the test method and composition. The reduced porosity in the previous studies was consistently lower than 30% [10]. Even with high porosity, the present results indicate that Ni–YRSZ anode supports retain adequate strength.

3.5. Gas transport and catalytic activity

Gas transport and catalytic reforming activity play important roles in anode-support structures. The “Separated Anode Experiment” is designed specifically to characterize these processes in cermet anodes [11], while decoupling them from the electrochemical processes underway in complete cells. As illustrated in Fig. 6, a planar anode disk is pressed between two steel fixtures across which flow channels have been machined. The entire assembly is placed within a furnace and heated to SOFC operating temperatures (600–800 °C). The “fuel channel” is supplied with gas mixtures that represent SOFC fuels, and the “electrolyte channel” is supplied with gas mixtures that represent the composition at the anode triple-phase boundaries (i.e., reaction products steam and carbon dioxide). Both channels carry the reactive flow in a reducing carrier gas (3.5% H_2 in Ar) to prevent nickel oxidation. The Ar also assists in calibrating gas-composition measurements.

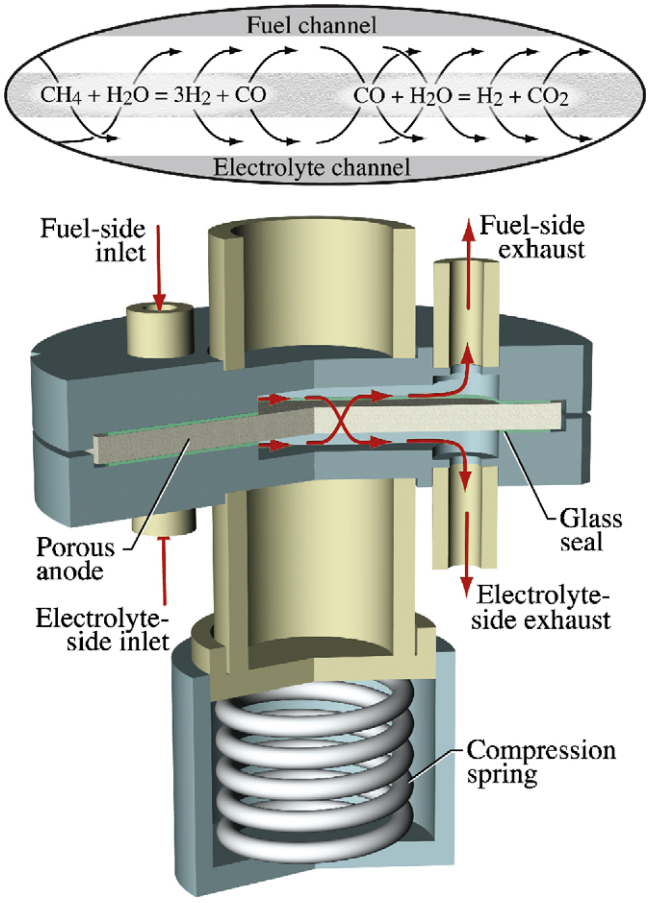

Fig. 6. Schematic of the Separated Anode Experiment. The balloon illustrates the directions of species fluxes associated with on-anode reforming.

Gases from both the fuel and electrolyte channels are free to diffuse through the porous anode and to participate in heterogeneous reforming reactions. By varying the inlet flow rates, the relative effects of transport and chemical reaction can be studied. The exhaust-gas compositions from both channels are measured using a mass spectrometer (Stanford Research Systems RGA 200). The composition measurements are interpreted by computational models that represent fluid flow, porous-media transport, and elementary catalytic chemistry [11].

The models are previously documented, so only a brief summary is included here [11]. Both channel flows are modeled using steady-state plug-flow assumptions. That is, the overall and species continuity equations are

$$\frac{\mathrm{d}(\rho u)}{\mathrm{d}x} = \frac{P}{A_c}\sum_{k=1}^{K} J_k W_k, \quad \frac{\mathrm{d}(\rho u Y_k)}{\mathrm{d}x} = \frac{P}{A_c} J_k W_k. \tag{1}$$

In these equations the independent variable is x, the distance along the channels. The dependent variables are the flow velocity u and mass fractions Y_k of the K gas-phase species. The species molecular weights are written as W_k. The width of the channel is represented as P and the channel cross-sectional area is A_c. The variables J_k represent the normal component of the species molar fluxes at the interfaces between the flow channels and the porous anode structure. The exchange fluxes are determined by solving a reactive porous-media problem within the anode. The behavior within the anode is described compactly by

$$\nabla \cdot \mathbf{J}_k = A_s \dot{s}_k, \tag{2}$$

Table 1
Heterogeneous reaction mechanism that describes CH_4 reforming on Ni-based catalysts.

$H_2(g) + (Ni) + (Ni) \leftrightharpoons H(Ni) + H(Ni)$
$O_2(g) + (Ni) + (Ni) \leftrightharpoons O(Ni) + O(Ni)$
$CH_4(g) + (Ni) \leftrightharpoons CH_4(Ni)$
$H_2O(g) + (Ni) \leftrightharpoons H_2O(Ni)$
$CO_2(g) + (Ni) \leftrightharpoons CO_2(Ni)$
$CO(g) + (Ni) \leftrightharpoons CO(Ni)$
$O(Ni) + H(Ni) \leftrightharpoons OH(Ni) + (Ni)$
$OH(Ni) + H(Ni) \leftrightharpoons H_2O(Ni) + (Ni)$
$OH(Ni) + OH(Ni) \leftrightharpoons O(Ni) + H_2O(Ni)$
$O(Ni) + C(Ni) \leftrightharpoons CO(Ni) + (Ni)$
$O(Ni) + CO(Ni) \leftrightharpoons CO_2(Ni) + (Ni)$
$HCO(Ni) + (Ni) \leftrightharpoons CO(Ni) + H(Ni)$
$HCO(Ni) + (Ni) \leftrightharpoons O(Ni) + CH(Ni)$
$CH_4(Ni) + (Ni) \leftrightharpoons CH_3(Ni) + H(Ni)$
$CH_3(Ni) + (Ni) \leftrightharpoons CH_2(Ni) + H(Ni)$
$CH_2(Ni) + (Ni) \leftrightharpoons CH(Ni) + H(Ni)$
$CH(Ni) + (Ni) \leftrightharpoons C(Ni) + H(Ni)$
$O(Ni) + CH_4(Ni) \leftrightharpoons CH_3(Ni) + OH(Ni)$
$O(Ni) + CH_3(Ni) \leftrightharpoons CH_2(Ni) + OH(Ni)$
$O(Ni) + CH_2(Ni) \leftrightharpoons CH(Ni) + OH(Ni)$
$O(Ni) + CH(Ni) \leftrightharpoons C(Ni) + OH(Ni)$

where $\mathbf{J}_k$ are the species fluxes within the anode, A_s is the specific area (i.e., area per unit volume) of the exposed Ni catalyst, and $\dot{s}_k$ are the molar production rates of gas-phase species k by heterogeneous reforming chemistry [12]. The species fluxes within the porous anode are governed by the Dusty-Gas Model (DGM) [13,14], which is an implicit relationship among the gas-phase species molar fluxes $\mathbf{J}_k$, molar concentrations $[X_k]$, concentration gradients, and the pressure p gradient as

$$\sum_{\ell \neq k} \frac{[X_\ell]\mathbf{J}_k - [X_k]\mathbf{J}_\ell}{[X_T]D^e_{k\ell}} + \frac{\mathbf{J}_k}{D^e_{k,Kn}} = -\nabla[X_k] - \frac{[X_k]}{D^e_{k,Kn}}\frac{B_g}{\mu}\nabla p. \tag{3}$$

In this expression $[X_T] = p/RT$ is the total molar concentration, B_g is the permeability, and μ is the mixture viscosity. This model represents the combined effects of ordinary multicomponent diffusion, Knudsen diffusion, and pressure-driven Darcy flow. The effective ordinary and Knudsen diffusion coefficients $D^e_{k\ell}$ and $D^e_{k,Kn}$ depend on the binary diffusion coefficients (evaluated from kinetic theory) and physical properties of the porous media, including porosity, average pore radius r_p, and tortuosity τ_g.

The heterogeneous reaction mechanism that describes Ni-based reforming kinetics is taken from Hecht et al. [11]. Although details are documented elsewhere, Table 1 is included to emphasize the fundamental nature of the reaction chemistry. This mechanism, which involves 21 reversible elementary reactions among 6 gas-phase and 12 surface-adsorbed species, has been validated experimentally for both steam and dry (CO_2) reforming within Ni–YSZ anodes at 800 °C. Because the elementary reaction mechanism describes all combinations of steam reforming, dry reforming, partial oxidation, and autothermal reforming, it is far more powerful than the global steam-reforming mechanisms that are often used in SOFC modeling. Gas-phase chemistry within the channels and the anode pore space is assumed to be negligible.

The Separated Anode Experiment is used initially to evaluate gas transport through the C- and RS-based anodes. In this case, inert-gas streams are used. The electrolyte-inlet stream is a mixture of CO_2 and reducing gas (3.5% H_2 in Ar) and the fuel-inlet stream is supplied with only reducing gas. The CO_2 diffuses across the anode from the electrolyte side to the fuel side. Thus, the CO_2 mole fraction in the fuel exhaust is indicative of gas transport through the anode support under test. Measurements are conducted with electrolyte-inlet mole fractions of 33%, 48% and 61% CO_2. The total flow rate is equal in each channel and held constant at 100 sccm.

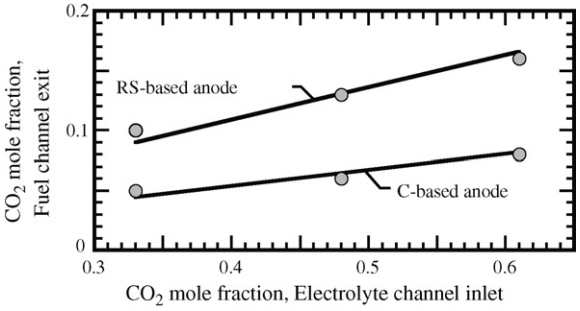

Fig. 7. Experimental (symbols) and modeling (lines) results of inert gas transport across C- and RS-based anodes. CO_2 mole fraction in fuel-exhaust streams are plotted as functions of CO_2 mole fraction in electrolyte-inlet stream.

Fig. 7 shows results of the transport experiments compared with model predictions. The CO_2 mole fraction in the fuel-side exhaust is consistently higher (nearly double) for the RS-based anode. This result highlights the more facile gas transport through RS-based anodes compared to the conventional anode. The results is also consistent with the more-open microstructure as seen in the microscopic images (Fig. 3). The model is used to infer difficult-to-measure parameters such as the tortuosity τ. Results indicate that the C-based anode tortuosity is $\tau_C = 3.5$ and the RS-based anode tortuosity is $\tau_{RS} = 2.3$. The lower tortuosity for the RS-based anode is again consistent with more-open pore structure seen in the SEM images and porosimetry measurements.

In addition to facilitating transport of reactants and products to and from the electrochemically active three-phase boundaries, SOFC anodes must also promote internal reforming of hydrocarbon fuels. To compare the catalytic activity of C- and RS-based anodes, chemically reactive gas streams are introduced in the Separated Anode Experiment. The results shown in Fig. 8 are for a fuel inlet mixture of 20% CH_4 and 80% reducing gas and an electrolyte-side inlet mixture of 25% CO_2, 25% H_2O, and 50% reducing-gas. The methane diffusing through the anode reacts with the counter-diffusing CO_2 and H_2O on the catalytic nickel surface, forming CO and H_2.

Fig. 8 shows H_2 and CO mole fractions in the electrolyte-side exhaust as functions of the inlet flow rates, with both channels having the same flow rates. The RS-based anode clearly shows higher reforming activity than the C-based anode. As should be anticipated, increasing flow rates decreases residence time and thus

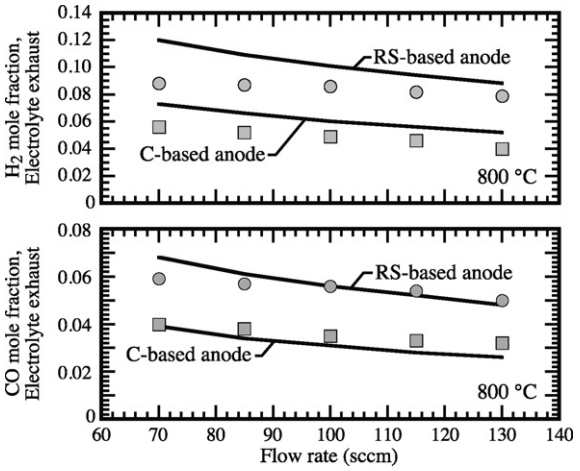

Fig. 8. H_2 and CO mole fractions in the separated anode electrolyte-channel exhaust as functions of inlet flow rates. Experimental measurements (symbols) are compared with modeling predictions (lines).

diminishes the reforming performance. The model predicts the CO performance well, but is qualitatively less predictive for the H_2. In both cases, the model predicts the observed trends.

These results show that the catalytic activity of the RS-type anodes is at least equivalent to that of the conventional anodes. Therefore, it is anticipated that SOFC performance should be enhanced as a result of higher H_2 and CO reaching the electrochemically active three-phase boundaries near the dense-electrolyte interface. Transport of reaction products (H_2O and CO_2) away from the triple-phase boundaries should be more facile in RS-based anodes. All of these results suggest that YRSZ anodes should perform at least equivalently to, and perhaps better than, the conventionally processed anodes.

3.6. Electrochemical performance

Electrochemical performance of tubular membrane–electrode assemblies fabricated using RS- and C-based anodes is measured and compared. The complete cells are operated in a furnace at a uniform temperature of 800 °C. Initial heating from room temperature is at a rate of 120 °C h^{-1}. Humidified hydrogen (3% water vapor) is supplied to the cell by bubbling hydrogen through a room-temperature water bath. The cathode (outside of the tube) is simply exposed to air within the furnace. Each SOFC tube is connected to the gas manifold and electrical components using cold-zone, compression-style fittings and silicone tubing to establish reactive-gas sealing and electrical isolation. Anode current collection is accomplished by wrapping nickel mesh around solid 18 AWG and 22 AWG nickel wires; this bundle is then inserted within the inner diameter of the tubular SOFC, establishing contact with the anode surface. Cathode current collection is accomplished using 22 AWG silver wire to adhere more-robust 18 AWG silver wires to the surface of the LSM-YSZ cathode. A thin layer of silver paste is applied over the entire cathode surface and at the interface between the cathode and the silver wires.

During start-up heating, the anode is supplied with a stream of dilute reducing gas (125 sccm) until the SOFC is stable at 800 °C. Once the operating temperature is achieved, the fuel stream switches to 200 sccm of industrial-grade hydrogen. After establishing a stable open-circuit voltage (OCV), an automated load cell (Chroma, 63103) is used to measure polarization characteristics. Electrochemical Impedance Spectra (EIS) are also measured using a Gamry Instruments—Reference 600 Potentiostat/Galvanostat. The frequency range of the impedance measurement is 0.1 Hz to 10 kHz. Data acquisition is controlled using National Instruments hardware and LabView software.

Fig. 9a shows measured polarization characteristics of an RS-based and a C-based MEA. Open-circuit potentials of about 1.1 V for both cells indicates that there are minimal leaks through the electrolyte. The cells have nearly identical polarization curves until higher current densities are reached (0.45 W cm^{-2}), above which the C-based potential drops rapidly. The delay in the onset of high concentration polarization is in keeping with the more open morphology and higher gas transport displayed by the RS-based anodes.

Peak power densities of about 0.30 W cm^{-2} are achieved at a cell potential of 0.48 V for both cells. In other similarly fabricated RS-based cells, peak power of 0.5 W cm^{-2} was achieved. Such performance is clearly lower than the best-in-class button cells that achieve power densities approaching 2.0 W cm^{-2} [15–17]. However, the objective here is to evaluate alternative anode-fabrication techniques, not to develop a top-performing cell. Thus, there was no systematic attempt to optimize the membrane–electrode assembly to achieve high power. The results show that the Ni–YRSZ cell performs comparably to an equivalent cell with the anode fabricated using conventional methods. Certainly architectural and materials improvements, such as electrode functional layers and improved

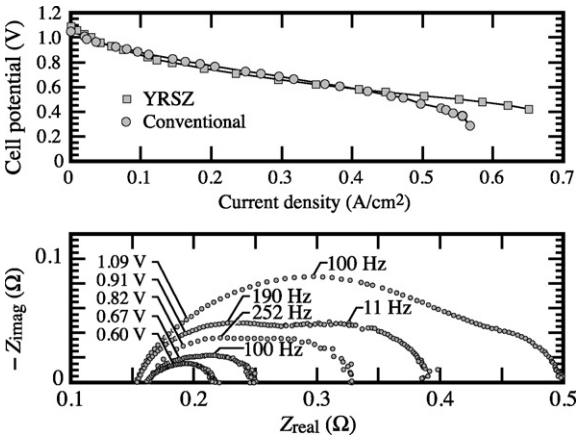

Fig. 9. Electrochemical performance of slip-cast tubular SOFC fabricated with RS- and C-based anodes at 800 °C under humidified hydrogen: (a) polarization curves and (b) electrochemical impedance response.

electrocatalysts (especially for the cathode), would improve performance in both cases.

Fig. 9b shows EIS measurements from an RS-based MEA. As cell voltage is decreased, cathode activation losses begin to dominate the impedance spectra. These results indicate that cell electrochemical performance could be further increased through use of advanced cathode materials and structures, and that cell performance is not hindered through use of reaction-sintered YSZ anode material.

4. Conclusion

This paper reports on the fabrication and performance of solid-oxide fuel cell anodes employing yttria reaction-sintered zirconia (YRSZ). Through the reaction-sintering process, the technical-grade YSZ commonly used in the Ni–YSZ anode cermet is replaced with lower-cost ZrO_2 and Y_2O_3 materials. When sintered in the presence of nickel oxide, ZrO_2 and Y_2O_3 form cubic-phase YSZ at temperatures characteristic of SOFC fabrication (1400–1550 °C). Reaction sintering enables the formation of YSZ during cell fabrication, reducing SOFC anode raw-materials cost and the number of SOFC-fabrication processes. Direct structural and microstructural comparisons of conventionally fabricated anodes and YRSZ anodes suggest that the YRSZ material is comparable to conventionally fabricated anodes. X-ray diffraction shows that reaction sintering achieves the desired material phases and crystal structures. Mechanical strength and electronic conductivity are comparable to anodes that are produced by conventional methods. Gas-phase transport and catalytic reforming activity in the YRSZ anodes are comparable to, or better than, the conventional materials. Electrochemical performance of full cells is reasonable, but can be improved by development of functional layers and higher-performance cathodes. Overall, the YRSZ process promises high-performance cermet anodes at reduced fabrication costs.

Acknowledgments

This work has been funded in part by the Office of Naval Research, Multidisciplinary University Research Initiative, Contract Number N00014-02-1-0665, and by the Department of Energy, Office of Energy Efficiency and Renewable Energy, Contract Number DE-FG36-08GO88100. Special thanks given to Eva Salas, undergraduate student at the Colorado School of Mines, for conducting electronic-conductivity experiments, and to Connor Moyer, graduate student at the Colorado School of Mines, for acquisition of SEM images.

References

[1] K.J. Yoon, P. Zink, S. Gopalan, U.B. Pal, J. Power Sources 172 (2007) 39–49.
[2] R. Swartzlander, W.G. Coors, Preparation of yttria-stabilized zirconia reaction sintered products, United States Patent 20,070,176,332 (2007).
[3] A. Kuzjukevics, S. Linderoth, Mater. Sci. Eng. A232 (1997) 163–167.
[4] M.K. Dongare, K. Malshe, C.S. Gopinath, I.K. Murwani, E. Kemnitz, J. Catal. 222 (2004) 80–86.
[5] A.A.E. Hanssan, N.H. Menzler, B. Blass, M.E. Ali, H.P. Buchkremer, D. Stover, J. Mater. Sci. 37 (2002) 3467–3475.
[6] J.S. Reed, Principals of Ceramics Processing, John Wiley and Sons, New York, 1995.
[7] Standard test methods for apparent porosity, water absorption, apparent specific gravity, and bulk density of burned refractory brick and shapes by boiling water. Technical Report C20-00, ASTM International, 2005.
[8] D.W. Dees, T.D. Claar, T.E. Easler, D.C. Fee, F.C. Mrazek, Electrochem. Sci. Technol. 139 (1987) 2141–2146.
[9] Standard test method for flexural strength of advanced ceramics at ambient temperature. Technical Report C1161, ASTM International, 2008.
[10] N.M. Sammes, Y. Du, J. Mater. Sci. 38 (2003) 4811–4816.
[11] E.S. Hecht, G.K. Gupta, H. Zhu, A.M. Dean, R.J. Kee, L. Maier, O. Deutschmann, Appl. Catal. A 295 (2005) 40–51.
[12] R.J. Kee, M.E. Coltrin, P. Glarborg, Chemically Reacting Flow: Theory and Practice, John Wiley, Hoboken, NJ, 2003.
[13] E. Mason, A. Malinauskas, Gas Transport in Porous Media: The Dusty-Gas Model, American Elsevier, New York, 1983.
[14] H. Zhu, R.J. Kee, V.M. Janardhanan, O. Deutschmann, D.G. Goodwin, J. Electrochem. Soc. 152 (2005) A2427–A2440.
[15] A.V. Virkar, J. Chen, C.W. Tanner, J.-W. Kim, Solid State Ionics 131 (2000) 189–198.
[16] Y. Lin, Z. Zhan, J. Liu, S.A. Barnett, Solid State Ionics 176 (2005) 1827–1835.
[17] F. Tietz, H.-P. Buchkreamer, D. Stover, J. Electroceram. 17 (2006) 701–707.